

# Unsupervised Depth Estimation, 3D Face Rotation and Replacement

Joel Ruben Antony Moniz<sup>1</sup> Christopher Beckham<sup>2,3</sup> Simon Rajotte<sup>2,3</sup> Sina Honari<sup>2</sup> Christopher Pal<sup>2,3</sup>

## Abstract

We present an unsupervised approach for learning to estimate three dimensional (3D) facial structure from a single image while also predicting 3D viewpoint transformations that match a desired pose and facial geometry. We achieve this by inferring the depth of facial key-points in an input image in an unsupervised way. We show how it is possible to use these depths as intermediate computations within a new backpropable loss to predict the parameters of a 3D affine transformation matrix that maps inferred 3D key-points of an input face to corresponding 2D key-points on a desired target facial geometry or pose. Our resulting approach can therefore be used to infer plausible 3D transformations from one face pose to another, allowing faces to be frontalized, transformed into 3D models or even warped to another pose and facial geometry. Lastly, we identify certain shortcomings with our formulation, and explore adversarial image translation techniques as a post-processing step. Correspondingly, we explore several adversarial image transformation methods which allow us to re-synthesize complete head shots for faces re-targeted to different poses as well as repair images resulting from face replacements across identities.

## 1. Introduction

Faces are a particularly important type of visual object as underscored by the fact that the human brain contains a specialized region for recognizing faces known as the fusiform face area. Correspondingly, facial pose normalization and pose-invariant face verification are both important and well studied problems in computer vision (Zhang & Gao, 2009; Taigman et al., 2014). Pose normalization for faces refers to the process of modifying an image of a face, often in order

to make it appear as if the person was directly looking into a camera located right in front of the face. This is sometimes referred to as frontalization (Hassner et al., 2015). Pose normalization can be an important pre-processing step leading to improved accuracy for face classifiers or verifiers (Taigman et al., 2014; Zhu et al., 2015; Tran et al., 2017; Huang et al., 2017), or when used as input to a wide variety of other facial analysis tasks. These tasks become much more difficult when a given face is not facing the camera.

We present a novel unsupervised learning technique for face rotation and warping from a single 2D image to a target face through estimating depth using neural networks. These neural networks use a novel loss formulation for the structured prediction of key-point depths. In our approach we first extract key-points from a source image, whose facial appearance will be used in the rotation. These key-points are mapped to a target face, where the facial pose and geometry inferred from the source image is mapped. More specifically, the key-points of the source image are first extracted and together with the key-points of the target face (which is taken from either a template face or extracted from an image) passed to a neural network to simultaneously estimate the depth of the source key-points and a 3D affine transformation matrix that maps the source key-points onto the target key-points. The base version of our approach uses only source and target key-points to infer depth and the global 3D transformation. We describe extended variants of the proposed model in Section 2 that take other inputs such as the original source and target images. Once the 3D affine transformation matrix is estimated, if desired, it can be used to warp the source image onto the target face geometry using a textured triangular mesh. The use of a 3D affine transform means that we can capture both a 3D rotation of the face to a new viewpoint as well as a global non-Euclidean warping of the geometry to match a target face. We call these neural networks Depth Estimation-Pose Transformation Hybrid Networks, or Depth-Nets in short.

We explore two types of Depth-Nets along with variations of these types. The first type uses a neural architecture to predict both the depth of source key-points as well as the parameters of a 3D geometric affine transformation which approximates a model for face mapping from source to target images. In this configuration of Depth-Nets both depth and affine transformation parameters are predicted at the

<sup>1</sup>School of Computer Science, Carnegie Mellon University

<sup>2</sup>MILA - University of Montreal <sup>3</sup>Ecole Polytechnique of Montreal.  
Correspondence to: Joel Moniz <jrmoniz@andrew.cmu.edu>, Sina Honari <honaris@iro.umontreal.ca>.

output of the Depth-Net model, forming different explicit predictions of the model. The predicted depth and affine transformation could be then used to map a source face to a target face for object orientation, distortion and viewpoint changes. The exploration of neural networks which simultaneously predict depth and affine transformation constitutes our first contribution.

Our second contribution consists of making the observation that given 3D source and 2D target key-points, closed form least squares solutions exist for estimating geometric affine transformation models between these sets of key-point correspondences, and we can therefore develop a model that captures the dependency between depth and the affine transformation parameters. More specifically, we express the affine transformation as a function of pseudoinverse transformation of 2D key-points in a source image - augmented by inferred depths - and the target key-points. Thus, the second and major contribution in this work is therefore the fact that with our formulation we are able to capture the relationship between estimated affine transformation and inferred depth as a deterministic relationship, without introducing extra parameters for the geometric affine transformation. In this formulation, Depth-Net only predicts depth values explicitly and the affine transformation parameters are indirectly estimated through pseudoinverse transformation of source and target key-points.

Occluded regions of any object will lead to distortions in the appearance of a target model due to limited texture information to be transferred from the source to the target pose. To repair such distortions, we use an adversarial image-to-image transformation approach on the Depth-Net outputs. Finally, our third contribution is the use of an adversarial unpaired image-to-image transformation approach to repair the appearance of 3D models inferred from a single image. Together these contributions allow 3D models of faces to be inferred from a single image. Our proposed method can be used for pose normalization which can serve as a pre-processing task for face verification with no manually specified 3D face model. To the best of our knowledge, this is the first such neural network based model that estimates a 3D affine transformation model for face rotation which neither requires ground-truth 3D images nor a ground truth 3D face information such as depth. We present the complete approach in detail below.

## 2. Our Approach

As we have outlined above, our approach consists of two main components: 1) Neural networks for inferring depth and geometric transformation – networks which we refer to as Depth-Nets; and, 2) An adversarial image-to-image transformation network which improves the quality of the appearance of a 3D model inferred from a Depth-Net. We

begin by describing our Depth-Net model in further detail, followed by a presentation of our image-to-image adversarial transformation approach.

### Depth-Nets

Our Depth-Net architectures are learned from key-points extracted from pairs of images, and (optionally) the original images themselves. We examine different neural architectures and loss variants by performing pose normalization based on inferring depths corresponding to 2D key-point locations as well as estimating affine transformation matrix. We do this by transforming the pose of one object or face, which we will refer to as the *source* to match that of the other, the *target* geometry. In all cases our models are not provided with any additional information about either an object or face's orientation or depth data.

1 - The first variation of our approach uses a neural network to predict both depths for each 2D point location in the source image and a corresponding 3D affine transform, both as *explicit* outputs of Depth-Net network. This process is performed using a transformation of 2D source key-points into 3-dimensional space using inferred depth, the model then applies the *predicted* 3D affine transform on them, and projects them back into 2D target space using an orthogonal projection. Since the points have to be projected back to 2D space, the parameters of the affine transform take the form of a  $4 \times 2$  matrix,  $\mathbf{F}$ .

2- In the second variation of our approach, similar to the variation above we predict the depths and the transformation matrix during training, but at test time, we only use the depth estimated by Depth-Net model and perform a second least squares estimation to determine the parameters of an affine transformation to map the 3D key-points to the 2D target geometry. The second step solves the least square estimation separately for each test example.

3- In the third variant of our approach we make the observation that there exists a closed form solution for estimating the 3D affine geometry that is consistent with a given 3D key-point configuration and we explore an architecture where we *backpropagate through this solution during learning*. In this approach the Depth-Net only estimates the depth values directly and the affine transformation parameters are obtained as a function of pseudoinverse transformation of 2D key-points and the estimated depth.

For each of the above three model variations above we explore two architectural scenarios: (A) a Siamese-like architecture that uses the source and target images themselves as well as key-points extracted from these images, and (B) a fully-connected neural network variant which uses only facial key-points in the source and target images. See Figure 1 for details.

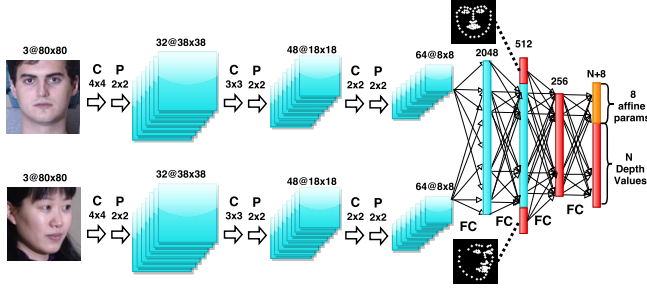


Figure 1. Depth-Net architecture. The blue region is only used in case (A) and the red part is used in both cases (A) and (B), described in Section 2. The orange output (the 8 affine transformation parameters) is predicted only by model variations #1 and #2 (described in Sections 2.1 and 2.2), and not the model variation #3 (described in section 2.3). All three model variations predict the  $N$  depth values of the source key-points. C, P, and FC correspond to valid conv, pool and fully-connected layers. The kernel size of the conv layer and the stride size of pool layer is mentioned on the corresponding arrows. The feature map size and the output size of FC layers are also indicated on top of the layers. The two paths of Siamese network share parameters and the black dots indicate concatenating key-point values to FC units.

The depths learned for each key-point by these approaches are not necessarily true depths, but are likely to strongly correlate with the actual depth of each key-point. This is because even though the method succeeds (as we shall see below) in aligning poses, the inferred depth and the affine transform may each be scaled by factors so as to cancel each other out (i.e., by factors which are multiplicative inverses of each other). Real world viewpoint geometry also involves perspective projection.

It is interesting to note that if Depth-Nets are used to register a set of images of objects to the same common viewpoint, the same image and geometry can be used as the target. This is the case for the frontalization of faces, for example. Here, our common target can either be the image of a front-facing face and the extracted key-points in the case of the Siamese variant (A) which uses both images and key-points, or a 2D key-point template in the case of the densely connected variant (B).

While the Depth-Net framework is sufficiently general to be applied to any object type where 2D key-point detections have been made, our experiments here focus on faces. Recombinator Networks (Honari et al., 2015) provide accurate detection for 2D facial key-point localization. Correspondingly, we begin by using them to extract 2D facial key-points. We describe mentioned variants of Depth-Nets in more details below.

## 2.1. Predicting Depth and Viewpoint Separately

In this variant of Depth-Nets, the model predicts both depths and viewpoint geometry, but as separate *explicit* outputs of a

neural network. The input is comprised of only the geometry and pose of the source and target faces (encoded in the form a 2D key-point template), case (B), or both key-points and images of the source and target faces, case (A). The key phases of this stage are described by the sequence of steps given below:

1. *Key-point extraction*: Raw (x, y) pixel coordinates corresponding to the key-points of each image are extracted using a Recombinator Network (RCN) (Honari et al., 2015) architecture, and then concatenated before being passed into the Key-point processing step.
2. *(Optional) Image Feature Extraction*: Depth-Nets can be conditioned on only key-points, case (B), or on key-points and the original images, case (A). We can therefore optionally subject the source and target images to alternating conv-maxpool layers. If this component of the architecture is used, the last spatial feature maps in the Siamese architecture are concatenated (as opposed to the more typical subtraction) before being given to a set of densely connected hidden layers.
3. *Key-point processing*: This step consists of the key-points being passed through a set of hidden layers. If the *Image Feature Extraction* stage of the pipeline is used, the key-points are concatenated to image features, the output of which is in turn fed to densely connected layers. The output layer of this phase will be of size  $N + 8$ , where  $N$  is the number of key-points. The first  $N$  points represent the Depth proxy, and the last 8 points a  $4 \times 2$  matrix representing the learned parameters of the affine transform. See Figure 1.
4. *Geometric Affine Transformation Normalizer*: This phase applies the predicted affine transform on each (depth augmented) source key-point to obtain its target location. Let  $(x_s^i, y_s^i)$  represent the  $i^{\text{th}}$  source key-point,  $(x_n^i, y_n^i)$  the corresponding source normalized key-point, estimated by applying the affine transformation matrix,  $(x_t^i, y_t^i)$  the  $i^{\text{th}}$  target key-point (as ground truth), and  $I_s$  and  $I_t$  represent the source and target images respectively. Depending on which underlying architectural variant we use (which effectively amounts to whether or not the chosen architecture performs the *Image Feature Extraction* step), two cases arise: one that utilizes only the key-points (B), and the other utilizing both the key-points and the images (A). Since the key-points are generated using RCNs, they are technically functions of the input images:  $[x_s, y_s] = \mathbf{R}(I_s)$ , and  $[x_t, y_t] = \mathbf{R}(I_t)$ . Depending on the variant, the  $i^{\text{th}}$  key-point's predicted depth proxy  $z_p^i$  is inferred as a function of the input key-points, or both input key-points and input images. The key-points in turn being derived from the images, we get  $z_p^i = z_p^i(I_s, I_t)$  in both cases. Similarly, the 3D-2D affine transform  $\mathbf{F}$  is a function of the input points or of both the input points and images, such that  $\mathbf{F} = \mathbf{F}(I_s, I_t)$ , with each of the 8 predicted parameters

given by:  $\mathbf{m} = \{m_1, m_2, m_3, t_x, m_4, m_5, m_6, t_y\}$ . These constitute the 3D-2D affine transform which is common to all key-points. In other words, each of the  $i$  points is transformed using  $\mathbf{x}_n^i = \mathbf{F}(\mathbf{I}_s, \mathbf{I}_t) \mathbf{x}_s^i$ , or:

$$\begin{bmatrix} x_n^i \\ y_n^i \end{bmatrix} = \begin{bmatrix} m_1 & m_2 & m_3 & t_x \\ m_4 & m_5 & m_6 & t_y \end{bmatrix} \begin{bmatrix} x_s^i \\ y_s^i \\ z_p^i(\mathbf{I}_s, \mathbf{I}_t) \\ 1 \end{bmatrix}$$

Note, however, in the case of (B), when it uses a 2D key-point template in lieu of the target image key-points (for example, when normalizing a face to make it front-facing), the target is effectively hard-coded, and no longer forms a variable input. The predicted depth and affine then become functions purely of the source input image:  $\mathbf{z}_p^i = \mathbf{z}_p^i(\mathbf{I}_s)$  and  $\mathbf{F} = \mathbf{F}(\mathbf{I}_s)$ , respectively.

The loss function of a Depth-Net is obtained by transforming the source face to match the target face using the simple squared error of the corresponding target object's key-point vector  $\mathbf{x}_t = [x_t, y_t]^T$ , as ground truth values, and the source object's normalized key-point vector  $[x_n, y_n]^T$ , all normalized to the range  $[0, 1]$  by dividing with the total image size. The loss for one example where we predict depth and affine viewpoint geometry can therefore be expressed as:

$$\mathcal{L} = \sum_{i=1}^K \left\| \mathbf{x}_t^i - \mathbf{F}(\mathbf{I}_s, \mathbf{I}_t) [x_s^i \ y_s^i \ z_p^i(\mathbf{I}_s, \mathbf{I}_t)]^T \right\|^2 \quad (1)$$

**5. Image Warper:** This phase consists of using the depth proxy and affine transform matrix generated to actually warp the object or face from its source pose to be matched to the target object geometry. The final projection to 2D is achieved by simply dropping the transformed  $z$  coordinate (which corresponds to an orthographic projection model). In the case of Depth-Nets, this orthographic projection is effectively embedded in the *Geometric Affine Transformation Normalizer* step, since the affine corresponding to the  $z$  coordinate is not predicted, essentially dropping it.

As we operate on key-points, the actual warping of pixels can be performed with a high quality and high performance OpenGL pipeline that performs the warp separately from the rest of the architecture. Source Image, key-points augmented with depth, and the affine matrix are passed to OpenGL pipeline to warp the source image towards the target pose. This warping is not needed during training. A key advantage of using this formulation is that underlying imagery of arbitrarily high resolution can be processed with no impact on the complexity of depth and geometry prediction operations during training and test.

## 2.2. Estimating Viewpoint Geometry as a Second Step

In this model variant, training is similar to Section 2.1 and the model outputs depth and 3D affine transformation parameters. However, at test time, rather than using the predicted

3D affine transformation for pairs of objects, we use only the predicted depths and estimate the affine geometry parameters as a second estimation step. More precisely, given 3D points for a scene and the corresponding 2D points for a target geometry it is possible to formulate the estimation of a 3D affine transformation as a linear least squares estimation problem. An overdetermined system of the form  $\mathbf{A}\mathbf{m} = \mathbf{x}_t$  for this problem can be constructed as follows:

$$\begin{bmatrix} x_s^1 & y_s^1 & z_s^1 & 0 & 0 & 0 & 1 & 0 \\ 0 & 0 & 0 & x_s^1 & y_s^1 & z_s^1 & 0 & 1 \\ x_s^2 & y_s^2 & z_s^2 & 0 & 0 & 0 & 1 & 0 \\ 0 & 0 & 0 & x_s^2 & y_s^2 & z_s^2 & 0 & 1 \\ \vdots & & & & & & & \\ x_s^K & y_s^K & z_s^K & 0 & 0 & 0 & 1 & 0 \\ 0 & 0 & 0 & x_s^K & y_s^K & z_s^K & 0 & 1 \end{bmatrix} \begin{bmatrix} m_1 \\ m_2 \\ m_3 \\ m_4 \\ m_5 \\ m_6 \\ t_x \\ t_y \end{bmatrix} = \begin{bmatrix} x_t^1 \\ y_t^1 \\ x_t^2 \\ y_t^2 \\ \vdots \\ x_t^K \\ y_t^K \end{bmatrix} \quad (2)$$

This corresponds to an affine camera model followed by an orthographic projection to 2D. This setup also leads to the following closed form solution for the affine transformation parameters:

$$\mathbf{m} = [\mathbf{A}^T \mathbf{A}]^{-1} \mathbf{A}^T \mathbf{x}_t, \quad (3)$$

where this pseudoinverse based transformation is parameterized by the reference points and their predicted depths.

## 2.3. Joint Viewpoint and Depth Prediction

Our key observation is that one can alternatively use the closed form analytical solution, measured in Eq. (3), for the least squares estimation problem as the underlying affine transformation matrix within the loss function. This leads to a special form of structured prediction problem for geometrically consistent depths and affine transformation matrix. For each image we therefore have a loss of the form:

$$\begin{aligned} \mathcal{L} &= \sum_{i=1}^K \left\| \underbrace{\begin{bmatrix} x_t^i \\ y_t^i \end{bmatrix}}_{\mathbf{x}_t^i} - \underbrace{\begin{bmatrix} m_1 & m_2 & m_3 & t_x \\ m_4 & m_5 & m_6 & t_y \end{bmatrix}}_m \underbrace{\begin{bmatrix} x_s^i \\ y_s^i \\ z_p^i(\mathbf{I}_s, \mathbf{I}_t) \\ 1 \end{bmatrix}}_{\mathbf{x}_s^i} \right\|^2 \\ &= \sum_{i=1}^K \left\| \mathbf{x}_t^i - \text{reshape}[[\mathbf{A}^T \mathbf{A}]^{-1} \mathbf{A}^T \mathbf{x}_t] \mathbf{x}_s^i \right\|^2, \end{aligned} \quad (4)$$

where the matrix  $\mathbf{A}$  is parameterized as a function of  $\mathbf{x}_s$  as shown in (2). In this variant, the model *explicitly* outputs only depth values during train and test time. The affine transformation matrix in Eq. (4) is replaced by Eq. (3), which measures the affine transformation as a pure function of source and target key-points plus the inferred depth. The big different of this formulation compared to Sections 2.1 and 2.2 is that geometric affine transformation parameters are no longer predicted by Depth-Net during training and at both train and test time – it *solves* the least square loss through the pseudoinverse based transformation. Since  $z_s^i = \mathbf{z}_p^i(\{x_s^j, y_s^j, x_t^j, y_t^j\}_{j=1 \dots N})$  is predicted within the

analytical formulation of the solution to the least squares minimization problem, we can backpropagate through the *solution* of a minimization problem that depends on the predicted depths.

### Adversarial Image-to-Image Transformation

Inevitably, some of the frontalized face outputs from the Depth-Net geometry inference followed by textured mesh transformation look distorted. This happens due to the fact that when part of the face is obscured the appearance of surfaces of the face is unknown. To address this issue, we utilize CycleGAN (Zhu et al., 2017), a recently proposed adversarial image-to-image translation technique. This serves to repair the appearance of faces that have undergone frontalization through the Depth-Net pipeline. Importantly, the adversarial nature of CycleGAN allows one to perform image transformation between two domains without the requirement of paired data. In our work, we perform experiments translating between various domains of interest but one example is translating between the domain of frontal faces in the dataset (i.e. the ground truth) and the domain of faces that have been frontalized by Depth-Net. By learning a mapping from the latter to the former, we are able to perform a clean-up of these faces (if deemed necessary) with no requirement of extra supervisory signal (i.e. paired data).

Suppose we have some images belonging to one of two sets  $\mathbf{x} \in X$  (e.g. the DepthNet-frontalized faces) and  $\mathbf{y} \in Y$  (the ground truth faces which are frontal). We wish to learn two functions  $F : X \rightarrow Y$  and  $G : Y \rightarrow X$  which are able to map an image from one set to the corresponding image in the other. Correspondingly, we have two discriminators  $D_X$  and  $D_Y$  which try to detect whether the image in that particular set is real or generated. Note that while we are only really interested in the function  $F$ , the formulation of CycleGAN requires that we learn mappings in both directions during training since the irrelevant mapping is inherently linked to the one we are interested in. (We refer the reader to the appendix for the precise formulation of the algorithm.)

One can also easily condition on extra information without changing the formulation of the GAN. For example, instead of  $\mathbf{x}$  being the DepthNet-frontalized image, it could also be a channel-wise concatenation of that plus the background of the original pre-frontalized image, which CycleGAN could leverage to produce better predictions in the corresponding domain. As we will see later in this work, CycleGAN turns out to be quite a versatile post-processing technique for various tasks achieved with the Depth-Net, due to the fact that it is an unsupervised image translation method.

## 3. Related Work vs. Our Approach

### 3.1. 3D Transformation and Faces

While there is a large literature on 3D facial analysis, many standard and well known techniques are not applicable to our setting here – consisting of estimating depths from a single input image. As an example, Morphable models (Blanz & Vetter, 1999) cover a wide variety of approaches which are capable of high quality 3D reconstructions, but such methods usually require 3D face scans or reconstructions from multi-view stereo to be assembled so as to learn complex parametric distributions over face shapes. Our single image setting also eliminates many other standard computer vision techniques from being applicable, such as structure from motion methods.

One of the closest approaches to our own of which we are aware is that of (Hassner, 2013) on viewing real world faces in 3D. Like our work this approach does not require aligned 3D face scans, highly engineered models or manual interventions. In his work they make the observation that if 2D key-points can be obtained from a single input image of a face then if these key-points are matched to an arbitrary 3D target geometry, then standard camera calibration techniques can be used to estimate plausible intrinsics and extrinsics of the camera. This allows the estimated camera matrix, 3D rotation matrix and 3D translation vector to be used to transform the target 3D model to the pose of the query image from which an approximate depth can be obtained. (Hassner, 2013) then bridges the difference between the depth estimate obtained from the spatially transformed target model and the query face using a coordinate descent based joint depth and appearance optimization. Some more recent work has explored the use of a single unmodified 3D surface as an approximation to the shape of all input faces (Hassner et al., 2015). In contrast, in our approach we only require 2D keypoints from a source face and 2D keypoints for an arbitrary target face as input. We measure the depth of the source face keypoints, thereby inferring an image specific 3D model of the face. We also (simultaneously) infer a 3D affine transformation that captures viewpoint and facial keypoint geometry changes required to map the source face to the target. Our approach therefore allows for the immediate re-targeting of the inferred 3D model of the source face to the target face viewpoint and facial geometry. The work in (Hassner et al., 2015) also underscored the issue of visibility when faces are not frontal facing. In our work this issue manifests as incorrect appearance information obtained from pixels used for the initial texturing of a 3D mesh. We address the issue in our work here using an adversarial image repair technique.

In the high profile DeepFace work of (Taigman et al., 2014), the authors focused extensively on face frontalization to improve the performance of a face verification system. They

first detect, crop and align a face in-plane. They use a 3D mask composed of facial key-points, detect the corresponding locations of these key-points in the image, and map the 3D model onto the plane of the face. They then use this model to do a piecewise-affine transform on the face to frontalize it. They follow an end-to-end architecture and add the frontalized face as an intermediate step, in which each location in each feature map learns a different set of weights. In contrast, we do not require a 3D target face model, we only require an arbitrary 2D target key-points – no target appearance or textured 3D model is needed. We also simply use an affine camera model to account for potentially dramatic differences in query versus target geometry. Also, in our model only parameters of one affine camera model is learned for the entire facial key-points, rather than separate, per-pixel set of weights. Our approach is therefore less tied to faces in particular and is applicable to any sort of object where 2D key-point locations can be placed into semantic correspondence and geometric warping under a 3D affine model.

Spatial Transformer Networks (STNs) (Jaderberg et al., 2015) work either directly on input data, or on intermediate representations, to enhance the spatial invariance of CNNs, and to improve invariance to rotations, scaling and warping. They do this by learning and applying an input-dependent backpropable affine transformation either directly on the input image, or on an intermediate representation of the image (generated after the input has been passed through a part of a CNN pipeline). While STNs represent an excellent step towards automating pre-processing tasks such as cropping and rotation, this model fails for a crucial aspect of the normalization: out-of-plane rotations.

### 3.2. Generative Adversarial Networks

There has undoubtedly been an abundant literature exploring generative adversarial networks, and for good reason – framing problems as games between adversaries can side-step the issue of having to explicitly devise loss functions, which can be laborious. Recent adversarial models (Huang et al., 2017; Tran et al., 2017) have explored face rotation using purely neural networks. TP-GAN (Huang et al., 2017) performs face frontalization through introducing several losses to preserve identity and symmetry of the frontalized faces. Their model requires pairs of images of the same identity to train such a frontalization model. DR-GAN (Tran et al., 2017) rotate faces to any target pose by using a discriminator that does also identity classification, to maintains identity of faces, in addition to predicting the target pose to verify accurate face rotation. While these models do pure face rotation of an input 2D face, our model can warp the input face to any other target face, allowing warping the input face to any other identity, with a different geometry and pose. Moreover, our model also estimates the 3D geometric

affine transformation parameters explicitly, allowing these parameters to be used later, e.g., for face texture swap.

A recent topic of interest in this realm has been image-to-image translation, in which one is interested in mapping between various domains of interest. Conditional adversarial image-to-image networks were proposed by (Isola et al., 2016) in which one has paired data between the two domains of interest, i.e., each image in the domain has a corresponding image in the codomain, and a generator is learned to map from one domain to another is learned. Clearly however a limitation of this technique is its requirement for paired data. To alleviate this issue, (Zhu et al., 2017) proposed CycleGAN, which performs image-to-image translation for unpaired data, though there were also other works of similar spirit (Kim et al., 2017; Yi et al., 2017).

## 4. Experiments

We explore the three variants of Depth-Nets described in Sections 2.1, 2.2, and 2.3, each with two architectural cases (A) and (B), depending on whether image features are used in addition to key-points or not. We also compare with a number of baselines. Results for the following models are shown in Table 1:

- Model 1 is based on registrations using a simple 2D affine transformation.
- In model 2 we generated a 3D average face template from the 3DFAW dataset (Jeni et al., 2016; Gross et al., 2010; Yin et al., 2008; Zhang et al., 2014; Jeni et al., 2017) by aligning the 3D key-points of all faces in the dataset to a front-facing face using Procrustes superimposition. We report error by mapping the template face to each source face via Procrustes superimposition (to get  $f$ ) and then use an affine transformation from the 3D face  $f$  to the target face.
- For models 3 and 4 we use our proposed approach to predict both depth and geometry (described in Sections 2.1),
- Models 5 and 6 predict depth and visual geometry at training time, but then perform a secondary optimization to determine the optimal geometry at test (described in Section 2.2). Note that during training, these two cases are similar to models 3 and 4 in Table 1 and only at test time the formulation is different. So, the models in 3 and 4 are used to predict depth values at test time.
- Finally for models 7 and 8 we express the complete visual geometry estimation solution analytically as a function of the predicted depths within the loss, allowing backpropagation through the procedure (described in Section 2.3).

We provide more details about the experimental setup below.

Model	Color	MSE	MSE_norm
1) A simple 2D affine registration	grey	1.562	9.547
2) A 3D affine registration model using an average 3D face template	purple	0.724	7.486
3) A Depth-Net that separately estimates depth and geometry	brown	0.568	6.292
4) The model above, but with a Siamese CNN image model	violet	0.539	6.115
5) Secondary least squares estimation for visual geometry using the depths from 3)	red	0.400	5.184
6) Secondary least squares estimation for visual geometry using the depths from 4)	green	0.399	5.175
7) Backpropagation through the pseudoinverse based solution for visual geometry	orange	0.357	4.932
8) The model above, but with a Siamese CNN image model	blue	0.349	4.891

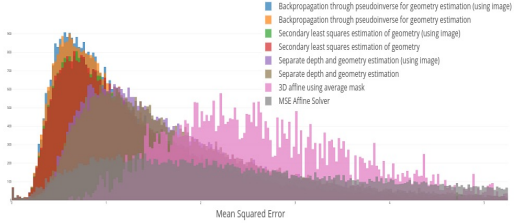


Table 1. (left) Comparing the Mean Squared Error (MSE) and MSE normalized by inter-ocular distance (MSE\_norm) of Different Models. (right) Histogram of Mean Squared Errors. The second column in the Table (on left) corresponds to the color of the model in the figure (on right).

#### 4.1. Image Registration

Our Depth-Net architectures require key-points of both source and target images in a pair to be extracted. For this, the image is first passed through the VGG-Face (Parkhi et al., 2015) face detector. The face crops are then scaled down to the size  $80 \times 80$  and converted to greyscale, following which they are passed through the RCN to obtain  $N = 68$  key-points on each image. The RCN is trained exactly as described in (Honari et al., 2015), using the 300W dataset (Sagonas et al., 2013).

The key-point only variant of our model involves concatenating all detected key-points and passing them through a two-layer deep fully connected network, with 256 hidden and  $o$  output units respectively, where  $o$  depends on whether we are predicting only the depth, when  $o = N$ , or the depth and an affine transform as well, when  $o = N + 8$ .

As discussed above, it is possible to augment these models with a Siamese CNN module (case A). For our exploration here model variants that also use the image pass both the source and the target images through three conv-maxpool ((32, 4, 2), (48, 3, 2), (64, 2, 2) respectively for the representation (num\_filters, filter\_size, pool\_size), all filters being square) layers with shared weights. The output of this is concatenated (much like in a Siamese architecture, as in (Bromley et al., 1994), (Chopra et al., 2005)) before passing them into a 4-layered fully connected network (with respective output sizes 2048, 512, 256 and  $o$ ). The key-points are concatenated to the 512 units before being passed to the last two layers. See Figure 1 for illustration of the model. We explore these Siamese CNN augmented variants in Model 4, 6 and 8 in Table 1.

We set the initial learning rate of 0.001 and use a nesterov momentum optimizer (with a momentum of 0.9) in all our experiments. With the exception of the last layer, we initialize all weights using a Glorot initialization scheme (Glorot & Bengio, 2010), with the weights sampled from a uniform distribution. We use a ReLU gain (He et al., 2015), set all biases to 0, and apply a ReLU non-linearity after every layer. In the final output layer, we do not apply any non-linearity and initialize the weights to 0. The biases of units that repre-

sent depths are initialized to a random Normal distribution with  $\mu = 0$  and  $\sigma = 0.5$ , while those that form the predicted affine transform are initialized with the equivalent of a "flattened" identity transform. All models have been trained for 500 epochs.

We point out that except for a comparison between learning rates in the set 0.01, 0.001, 0.0001 over a few (less than 10) epochs to find a learning rate that the model seems to train well with, we have not performed a hyperparameter search, and anticipate that the performance of the model can be made *even* better by searching the hyperparameter space on a per model basis and by using deeper (or modified) architectures.

Unless otherwise specified, for the experiments described below, we use a subset of the VGG dataset (Parkhi et al., 2015), training and validating on all possible pairs of images belonging to the same identity for 2401 identities, with roughly 20 images per identity, yielding 322,227 train and 43,940 validation pairs).

#### 4.2. Visualizing Depth Predictions

In Figure 2 (left) we show the depths that have been inferred for randomly selected faces. They demonstrate close correspondence to the ground truth depth. Note that the estimated depth of each key-point is relative with respect to other key-points (since there is no ground truth depth during training) rather than showing depth with respect to a reference such as the camera. In Figure 2 (right) we compare the predicted depths from two randomly selected faces from the 3DFAW dataset ((Jeni et al., 2015), (Zhang et al., 2014), (Yin et al., 2008), (Gross et al., 2010)) with ground truth depths (which are provided with this dataset). We see that depth predictions on the x-axis match reasonably well with the ground truth depth on the y-axis, up to a scale factor. This unidentifiable scale factor is to be expected as we discussed above. Note that for this task, we retrain the model on the VGG dataset, but by using a version of our model that predicts 66 proxy depth values instead of 68. In this case, we generate the key-points as before, using an RCN trained on the 300W dataset, but we discard two key-points. It is useful to note that face contour points do not correspond exactly due to

different annotations used to train RCN compared to the ones in 3DFAW dataset, so some errors arise from this fact, and we show the graph without these points.

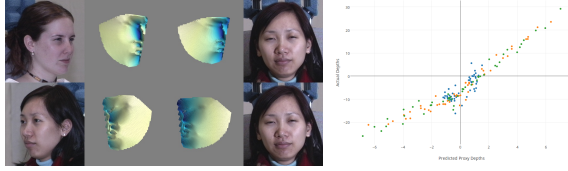


Figure 2. (left, top) Inferred depths for randomly selected pair and for same identity (left bottom). From left to right: source image; ground truth depth; inferred depth; target image. (right) Ground truth vs. predicted depths. l-to-f indicates left (as source) to front (as target) face rotation. r is a right posing face.



Figure 3. Visualizing the quality of depth predictions by re-projecting a frontal face (far left) to a range of other poses defined by the faces in the row above (in each pair of rows). In this experiment, we only use key-points from the top-row in the Depth-Net model (Model 7 in Table 1) that estimates the geometry of the target face for correct face mapping. Top two samples use different identities, while the last one uses the same person.

In Table 1 (right) we compare histograms of the mean squared error for the models given in the table on the left. As described at the start of the Experiments section, we train and test various versions of our model on a sub-set of the identities of the VGG dataset (with around 20 images present per identity), and measure the registration error (in the form of both the MSE and the Euclidean distance normalized by the intra-ocular distance, similarly to (Honari et al., 2015), for all possible pairs of faces belonging to the same identities in the respective sets. Thus, perfect registration should yield an error close to 0 – but not exactly zero since facial expressions may be different in each image. We see a clear progression as our models capture the interaction between depth estimation and visual geometry estimation and perform the estimation more directly.

In Figure 3 we visualize the quality of depth predictions by re-projecting a frontal face (far left) to a range of other

poses defined by the faces in the row above. The last row warps the frontal face on the left to each of the poses defined by other camera views of the same person allowing one to compare with a true view of the same person. These views are rendered from a 3D model in OpenGL. Images from Multi-PIE (Gross et al., 2010) are used for this experiment.

### 4.3. Face Replacement and Adversarial Repair

Here, we take a source and a target image and extract their key-points using a Recombinator Network. We pass the source and target through our Depth-Net to obtain the depth for each of the key-points in the source image and a global 3D affine transform to map the source to the target face. Pixels from the original source image are used to form the texture of a triangulated 2D mesh based on the key-points. The predicted depths are assigned to the key-points, with the depth of the points in between being interpolated, to form a 3D mesh, which is warped in 3D and orthographically projected to the target geometry using the predicted affine model for visual geometry. We then paste the rotated face by Depth-Net onto the background of the target image and train a CycleGAN to map from the domain of ‘swapped in faces’ to the ground truth faces in our dataset, effectively learning to clean up face swaps so that they are natural looking. Some examples of this procedure are shown in Figure 4. Note that in order to produce better translations, the dataset we used for all CycleGAN experiments is both the VGG dataset and the CelebA dataset, which has significantly more images.



Figure 4. (top row) Left to right: source face; target face; warp to target; repaired result. (bottom row) Warp to target and repair.

Secondly, we run some experiments where we use CycleGAN to add background detail to a face that has been frontalized with the Depth-Net architecture, so as to try and make it look indistinguishable from frontal faces in the dataset. We perform this in three different ways. Referring to Figure 5: in the first experiment (column 4) we condition the CycleGAN on the Depth-Net image (column 3) and the background of column 2 (masking interior face region determined by the convex hull spanned by the keypoints); in the second experiment (column 5) we map from only the original image (column 1); and in column 6 we condition on both the Depth-Net image and the original image. In all three cases, second domain contains ground truth frontal faces.

We describe the finer technical details of the CycleGAN architecture and training in the appendix. For now however,



Figure 5. Background synthesis with CycleGAN. Left to right: source face; keypoints overlaid; Depth-Net (DN); DN + background → frontal; source → frontal; source + DN → frontal

it suffices to say that we plan to experiment with more architectural variants for better translation quality.

## 5. Conclusion

We have proposed a novel neural network approach to 3D face model creation which enables relative pose normalization or frontalization without the use any ground truth depth data. We achieve our best quantitative key-point registration results using our novel formulation for predicting depth and 3D visual geometry simultaneously, learned through backpropagating through the analytic solution for the visual geometry estimation problem expressed as a function of predicted depths. We have illustrated the quality and utility of the depths and 3D transformations obtained using our method by transforming source faces to a wide variety of target poses and geometries. Our technique can also be used for face replacement and when combined with adversarial appearance repair it can blend warped faces to better match the appearance of the target. While the frontalization of side profile faces using this technique sometimes yields defects due to occlusions and keypoint localization errors, the output of Depth-Nets can be conditioned upon to help guide a GAN to re-synthesize faces in new poses in a controllable way. Our experiments indicate that defects of the 3D warping process tend to be repaired by this conditional adversarial generation procedure. Please see our supplementary material for additional examples.

## 6. Acknowledgment

We would like to thank Samsung for partially funding this project. We are also thankful to Compute Canada and Calcul Quebec for providing computational resources, and to Poonam Goyal for helpful discussions.

## References

Blanz, Volker and Vetter, Thomas. A morphable model for the synthesis of 3d faces. In *SIGGRAPH*, pp. 187–194, 1999. ISBN 0-201-48560-5.

Bromley, Jane, Guyon, Isabelle, LeCun, Yann, Säckinger, Eduard, and Shah, Roopak. Signature verification using a “siamese” time delay neural network. In *Advances in Neural Information Processing Systems*, pp. 737–744, 1994.

Chopra, Sumit, Hadsell, Raia, and LeCun, Yann. Learning a similarity metric discriminatively, with application to face verification. In *Computer Vision and Pattern Recognition, 2005. CVPR 2005. IEEE Computer Society Conference on*, volume 1, pp. 539–546. IEEE, 2005.

Glorot, Xavier and Bengio, Yoshua. Understanding the difficulty of training deep feedforward neural networks. In *International conference on artificial intelligence and statistics*, pp. 249–256, 2010.

Gross, Ralph, Matthews, Iain, Cohn, Jeffrey, Kanade, Takeo, and Baker, Simon. Multi-pie. *Image and Vision Computing*, 28(5): 807–813, 2010.

Hassner, Tal. Viewing real-world faces in 3d. In *Proceedings of the IEEE International Conference on Computer Vision*, pp. 3607–3614, 2013.

Hassner, Tal, Harel, Shai, Paz, Eran, and Enbar, Roe. Effective face frontalization in unconstrained images. In *Proceedings of the IEEE Conference on Computer Vision and Pattern Recognition*, pp. 4295–4304, 2015.

He, Kaiming, Zhang, Xiangyu, Ren, Shaoqing, and Sun, Jian. Delving deep into rectifiers: Surpassing human-level performance on imagenet classification. In *Proceedings of the IEEE International Conference on Computer Vision*, pp. 1026–1034, 2015.

Honari, Sina, Yosinski, Jason, Vincent, Pascal, and Pal, Christopher. Recombinator networks: Learning coarse-to-fine feature aggregation. *arXiv preprint arXiv:1511.07356*, 2015.

Huang, Rui, Zhang, Shu, Li, Tianyu, and He, Ran. Beyond face rotation: Global and local perception gan for photorealistic and identity preserving frontal view synthesis. In *The IEEE International Conference on Computer Vision (ICCV)*, Oct 2017.

Isola, Phillip, Zhu, Jun-Yan, Zhou, Tinghui, and Efros, Alexei A. Image-to-image translation with conditional adversarial networks. *CoRR*, abs/1611.07004, 2016. URL <http://arxiv.org/abs/1611.07004>.

Jaderberg, Max, Simonyan, Karen, Zisserman, Andrew, et al. Spatial transformer networks. In *Advances in Neural Information Processing Systems*, pp. 2008–2016, 2015.

Jeni, László A, Cohn, Jeffrey F, and Kanade, Takeo. Dense 3d face alignment from 2d videos in real-time. In *Automatic Face and Gesture Recognition (FG), 2015 11th IEEE International Conference and Workshops on*, volume 1, pp. 1–8. IEEE, 2015.

Jeni, László A, Tulyakov, Sergey, Yin, Lijun, Sebe, Nicu, and Cohn, Jeffrey F. The first 3d face alignment in the wild (3dfaw) challenge. In *European Conference on Computer Vision*, pp. 511–520. Springer, 2016.

Jeni, László A, Cohn, Jeffrey F, and Kanade, Takeo. Dense 3d face alignment from 2d video for real-time use. *Image and Vision Computing*, 58:13–24, 2017.

Kim, Taeksoo, Cha, Moonsu, Kim, Hyunsoo, Lee, Jung Kwon, and Kim, Jiwon. Learning to discover cross-domain relations with generative adversarial networks. *CoRR*, abs/1703.05192, 2017. URL <http://arxiv.org/abs/1703.05192>.

Parkhi, Omkar M, Vedaldi, Andrea, and Zisserman, Andrew. Deep face recognition. *Proceedings of the British Machine Vision*, 1 (3):6, 2015.

Sagonas, Christos, Tzimiropoulos, Georgios, Zafeiriou, Stefanos, and Pantic, Maja. 300 faces in-the-wild challenge: The first facial landmark localization challenge. In *Proceedings of the IEEE International Conference on Computer Vision Workshops*, pp. 397–403, 2013.

Taigman, Yaniv, Yang, Ming, Ranzato, Marc’Aurelio, and Wolf, Lior. Deepface: Closing the gap to human-level performance in face verification. In *Proceedings of the IEEE Conference on Computer Vision and Pattern Recognition*, pp. 1701–1708, 2014.

Tran, Luan, Yin, Xi, and Liu, Xiaoming. Disentangled representation learning gan for pose-invariant face recognition. In *Proceedings of the IEEE Conference on Computer Vision and Pattern Recognition*, 2017.

Yi, Zili, Zhang, Hao, Tan, Ping, and Gong, Minglun. Dualgan: Unsupervised dual learning for image-to-image translation. *CoRR*, abs/1704.02510, 2017. URL <http://arxiv.org/abs/1704.02510>.

Yin, Lijun, Chen, Xiaochen, Sun, Yi, Worm, Tony, and Reale, Michael. A high-resolution 3d dynamic facial expression database. In *Automatic Face & Gesture Recognition, 2008. FG’08. 8th IEEE International Conference on*, pp. 1–6. IEEE, 2008.

Zhang, Xiaozheng and Gao, Yongsheng. Face recognition across pose: A review. *Pattern Recognition*, 42(11):2876–2896, 2009.

Zhang, Xing, Yin, Lijun, Cohn, Jeffrey F, Canavan, Shaun, Reale, Michael, Horowitz, Andy, Liu, Peng, and Girard, Jeffrey M. Bp4d-spontaneous: a high-resolution spontaneous 3d dynamic facial expression database. *Image and Vision Computing*, 32 (10):692–706, 2014.

Zhu, Jun-Yan, Park, Taesung, Isola, Phillip, and Efros, Alexei A. Unpaired image-to-image translation using cycle-consistent adversarial networks. *CoRR*, abs/1703.10593, 2017. URL <http://arxiv.org/abs/1703.10593>.

Zhu, Xiangyu, Lei, Zhen, Yan, Junjie, Yi, Dong, and Li, Stan Z. High-fidelity pose and expression normalization for face recognition in the wild. In *Proceedings of the IEEE Conference on Computer Vision and Pattern Recognition*, pp. 787–796, 2015.

# Unsupervised Depth Estimation, 3D Face Rotation and Replacement: Supplementary Material

## 7. Additional Camera Sweep Visualizations

In this section, we present additional visualizations along the lines of those shown in Figure 3 in Section 4.2 of the main paper. Frontal faces selected from the Multi-PIE dataset (Gross et al., 2010) are re-projected to match several other poses corresponding to a person with a different identity. The Depth-Nets predicts accurate proxy depths, which when coupled with the analytically obtained affine transform (obtained from the least-squares pseudo-inverse-based solution described in Section 2.3 of the main paper) yields faces close to the desired target face geometry when passed through an OpenGL pipeline.



Figure 6. Visualizing the quality of depth predictions by re-projecting a frontal face (far left) to a range of other poses define by the faces in the row above.

We show camera sweeps for frontal source faces in Figures 6 and 7 and non-frontal source faces in Figures 8 and 9. Note that in the latter two Figures, the quality of images are reduced specially for frontal target faces. This is due to lack of adequate texture on the occluded side of the face to be transferred to the target pose by OpenGL pipeline, rather than inaccuracies in the affine transformation parameters. In order to reduce the side-affects, we use either of the source face or its flipped version, that is closer to the target face pose, and then warp the face to the target key-points.

In Figure 10 we visualize camera sweep for source faces in the wild that have more extreme poses. For this experiment we take source images from CelebA and frontalize it first by using Depth-Net. Since the frontalized faces have artifacts due to stretch of texture on the occluded side of the face by the OpenGL pipeline, we apply the adversarial repair to them. Finally we take the GAN-repaired frontalized faces and project it to target poses from the row above.

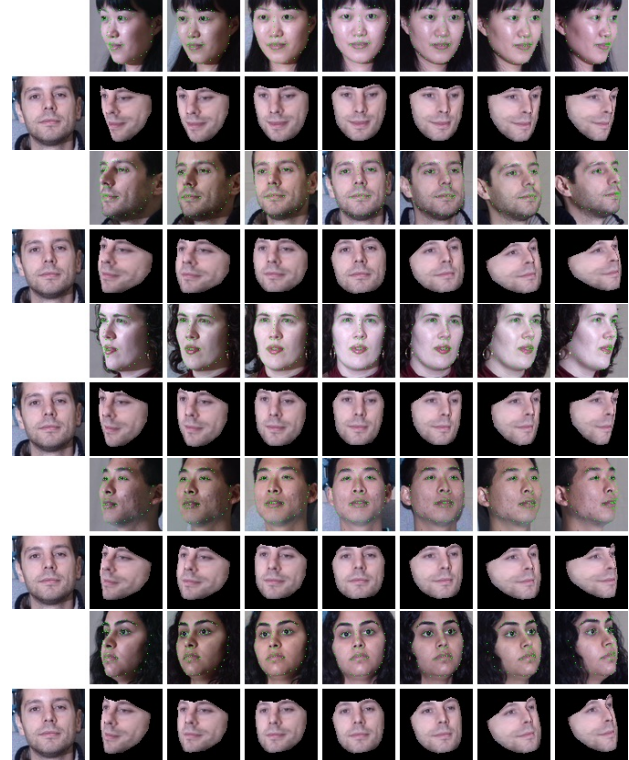


Figure 7. Visualizing the quality of depth predictions by re-projecting a frontal face (far left) to a range of other poses define by the faces in the row above.

## 8. CycleGAN

Suppose we have some images belonging to one of two sets  $\mathbf{x} \in X$  and  $\mathbf{y} \in Y$ , where  $\mathbf{x}$  denotes a a DepthNet-frontalized face and  $\mathbf{y}$  a ground truth face which is frontal. We wish to learn two functions  $F : X \rightarrow Y$  and  $G : Y \rightarrow X$  which are able to map an image from one set to the corresponding image in the other. Correspondingly, we have two discriminators  $D_X$  and  $D_Y$  which try to detect whether the image in that particular set is real or generated. As mentioned in the main text, while we are only interested in the function  $F : X \rightarrow Y$  (since this essentially tries to clean up the face and make it plausibly look like it came from



Figure 8. Re-projecting a non-frontal face (far left) to a range of other poses define by the faces in the row above. The bottom two camera sweeps use the same identity for source and target faces.



Figure 9. Re-projecting a non-frontal face (far left) to a range of other poses define by the faces in the row above. Here we use the same source face (far left) and warp it to different target identities.

the ground truth) the formulation of CycleGAN requires that we learn mappings in both directions during training. We optimize the

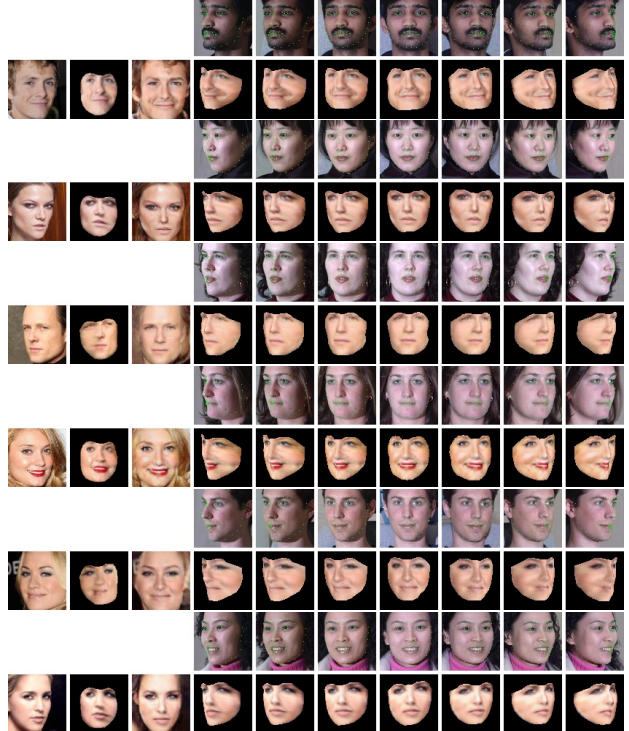


Figure 10. Re-projecting a non-frontal face (far left) from CelebA to a range of other poses define by the faces in the row above. Top row (in each pair) depicts the target faces from Multi-PIE. The bottom row shows from left to right: source face, source face frontalized by Depth-Net, adversarial-repaired face, the repaired source face projected to the target poses (4th to 10th columns).

following objectives for the two generators  $F$  and  $G$ :

$$\min_{G,F} \mathbb{E}_{\mathbf{x},\mathbf{y}} \left[ \ell(D_X(G(\mathbf{y})), 1) + \ell(D_Y(F(\mathbf{x})), 1) + \lambda \|\mathbf{y} - F(G(\mathbf{y}))\|_1 + \lambda \|\mathbf{x} - G(F(\mathbf{x}))\|_1 \right] \quad (5)$$

And the following for the two discriminators  $D_X$  and  $D_Y$ :

$$\min_{D_X,D_Y} \mathbb{E}_{\mathbf{x},\mathbf{y}} \left[ \ell(D_X(\mathbf{x}), 1) + \ell(D_X(G(\mathbf{y})), 0) + \ell(D_Y(\mathbf{y}), 1) + \ell(D_Y(F(\mathbf{x})), 0) \right], \quad (6)$$

where 0/1 denote fake/real,  $\ell()$  is the squared error loss and  $\lambda$  is a coefficient for the cycle-consistency (reconstruction) loss.

In the case where we condition on an extra image, the underlying math is exactly the same, only that this time  $\mathbf{x}$  is a channel-wise concatenation of the DepthNet-frontalized face and some extra conditioning image, such as the background of the original (pre-frontalized) image or even the whole original image itself. Once the network has been trained, we can disregard all other functions and use  $F$  to clean up faces which are low quality due to artifacts from warping.

In terms of architectural details the generators and discriminators used were those described in the appendix of the CycleGAN paper. In short, the generator consists of three conv-BN-relu blocks which downsample the input, followed by nine ResNet

blocks (which can be interpreted as iteratively performing transformations over the downsampled representation), followed by deconv-BN-relu blocks to upsample the representation back into the original input size. For training, we use the same hyper-parameters as most CycleGAN implementations which is using the Adam optimizer with learning rate  $\alpha = 2 \times 10^{-4}$ ,  $\beta_1 = 0.5$ ,  $\beta_2 = 0.999$ . However, instead of using a batch size of 1 we use the largest possible batch size, which was 16 for a 12GB GPU.

### 8.1. Background Synthesis

We present extra visualizations for the CycleGAN which performs background synthesis on CelebA, corresponding to Figure 5 in the main paper. These are shown in Figure 11. In terms of performance we observe that the model in column 4, which uses Depth-Net output plus the background information does better in terms of frontalizing the face, however, it does not preserve well the identity information. On the other hand, the models in columns 5 and 6 that use the ground truth face in the non-frontal pose, preserve better the identity of the person but suffer more in frontalizing the extreme poses. Comparing the models in columns 5 and 6, the model that uses both Depth-Net and the original face, yields more sharp results and has better contrast, while the model in column 5 that uses only the non-frontal ground truth input has more blurry results and hallucinates the projected face.

### 8.2. Face Replacement and Adversarial Repair

In Figure 12 we provide extra face swap samples on CelebA, corresponding to Figure 4 in the main paper, where a source face is warped to a target face pose using Depth-Net, pasted onto the target image and then passed to a CycleGAN to adapt the face skin of the warped source face to the background and hairstyle of the target face.

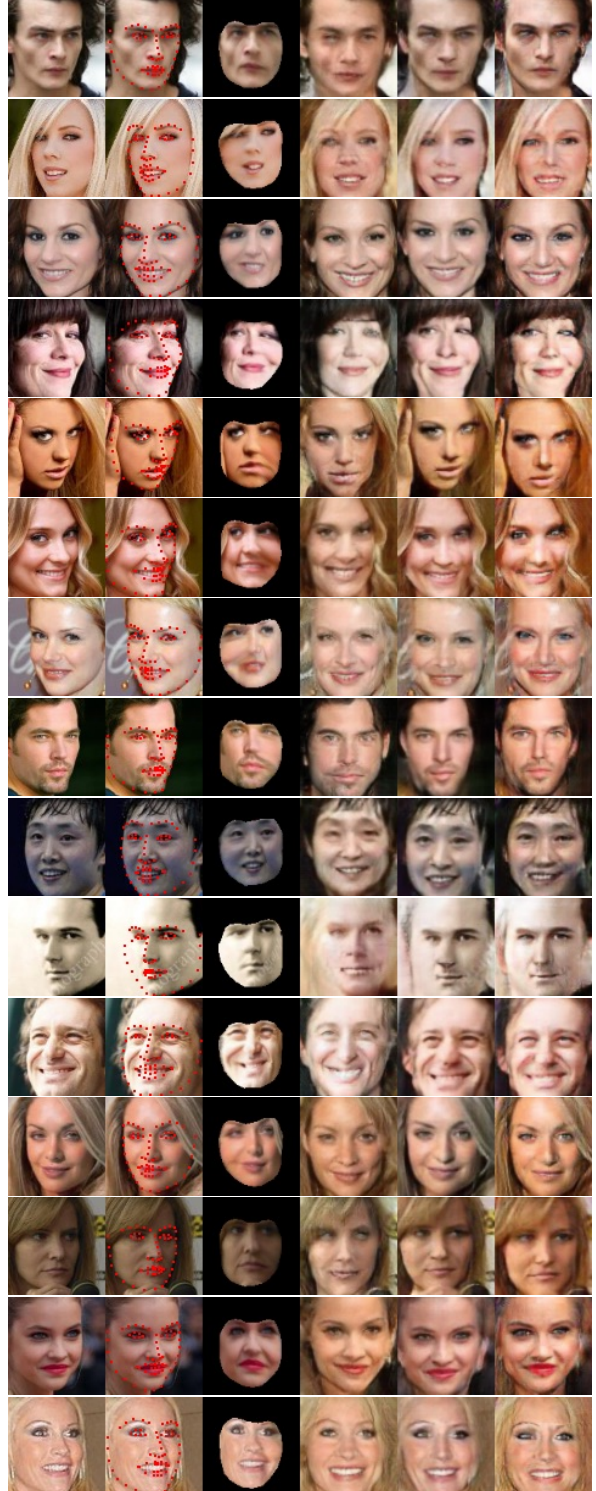


Figure 11. Background synthesis with CycleGAN. Left to right: source face; keypoints overlaid; Depth-Net (DN); DN + background → frontal; source → frontal; source + DN → frontal



Figure 12. Face swap experiment with CycleGAN. Left to right: source face; target face; warp to target with Depth-Net; repaired result with CycleGAN. The source face is taken and warped onto the target face. The background and hairstyle is then adapted to the target face.